# Viscous Core-Annular Flow in Microfluidic Chambers and Ultrafast Laser Microfabrication

A Thesis Presented

by

**Samira Darvishi**

to

The Graduate School

in Partial Fulfillment of the

Requirements

for the Degree of

**Master of Science**

in

**Mechanical Engineering**

Stony Brook University

**May 2011**

**Stony Brook University**

The Graduate School

**Samira Darvishi**

We, the thesis committee for the above candidate for the

Master of Science degree,

hereby recommend acceptance of this thesis.

**Dr. Thomas Cubaud, Advisor**
**Mechanical Engineering Department**

**Dr. Jon Longtin, Chair**
**Mechanical Engineering Department**

**Dr. David Hwang , Member**
**Mechanical Engineering Department**

This thesis is accepted by the Graduate School

**Lawrence Martin**
**Dean of the Graduate School**

Abstract of the Thesis

# Viscous Core-Annular Flow in Microfluidic Chambers and Ultrafast Laser Microfabrication

by

**Samira Darvishi**

**Master of Science**

in

**Mechanical Engineering**

Stony Brook University

**2011**

Microfluidic devices were utilized to study the behavior of highly viscous liquids surrounded by less viscous ones. This study mainly focuses on the lubrication transition of viscous threads flowing in sheaths of less viscous fluids, i.e., viscous core-annular flows. Miscible and immiscible fluid pairs with various viscosities, were tested in microchambers. A variety of flow patterns resulting from the viscous folding and capillary instabilities were observed and the relationships between flow morphologies and system parameters, including fluid viscosities, interfacial properties, flow rates of injection, and micro-cell geometry were examined.

In addition, in order to fabricate microchannels more efficiently, a femtosecond laser was used to study the potential of ultrafast laser micromachining. Three disparate materials were tested to establish the ablation abilities of the laser. Each test piece was etched multiple times with different powers and the consequential geometrical parameters (height and width) of each etched trench were measured. The final result was shown on one master curve that works as a guideline for micromachining of tapered channels in transparent materials.

# Contents

# List of Figures

# List of Tables

# 1 Introduction

Microfluidics- the study of fluids motion in micron and/or sub-millimeter scale structures- has been the hot topic in sciences since the late twentieth century. During the past fifteen years, advances in technology with microfluidic aids have grown drastically with applications in life sciences, and industries such as food and agriculture. The number of issued patents detailing the use of a microfluidic platform in a commercial application was less than 25 in 1998, yet in 2004 this number was over 350 [1]. Although there have been concerns about the high growth rates of microfluidic technology and lab-on-a-chip (LoC) systems [2–4], scientists and engineers are quite optimistic about the future of the field and hope for abundant usage of available technologies in industries while exploring new areas with these unique micro tools.

The advantages of microfluidics include, but are not limited to, small sample volumes leading to greater efficiency of chemical reagents; low production costs per device thereby allowing for disposability; high throughput synthesis and screening of biological species and drug targets; parallel processing of samples; fast sampling times; accurate and precise control of samples and reagents reducing the need for pipetting; low power consumption; and versatile format for integration of various detection schemes thereby leading to greater sensitivity [1].

A few examples of the main research areas in microfluidics are: biomedical detection and diagnostics [5–7], microreactors [8], micromixers [9], bubbles and droplet formations [10–16]. Interestingly, sometimes the side product of these microfluidic projects [17, 18] can even turn into an art piece (Figure 1) or trigger unique ideas such as designing games utilizing micro devices [19].

## 1.1 Motivation

Fluid motion in small scales plays an important role in our daily lives, from the blood circulation in our capillaries to the rise of sap in plants [20]. Microfluidics has provided a unique platform to study similar biological, physical and chemical phenomenon, as well as to produce remarkable solutions for affordable industrial products such as inkjet

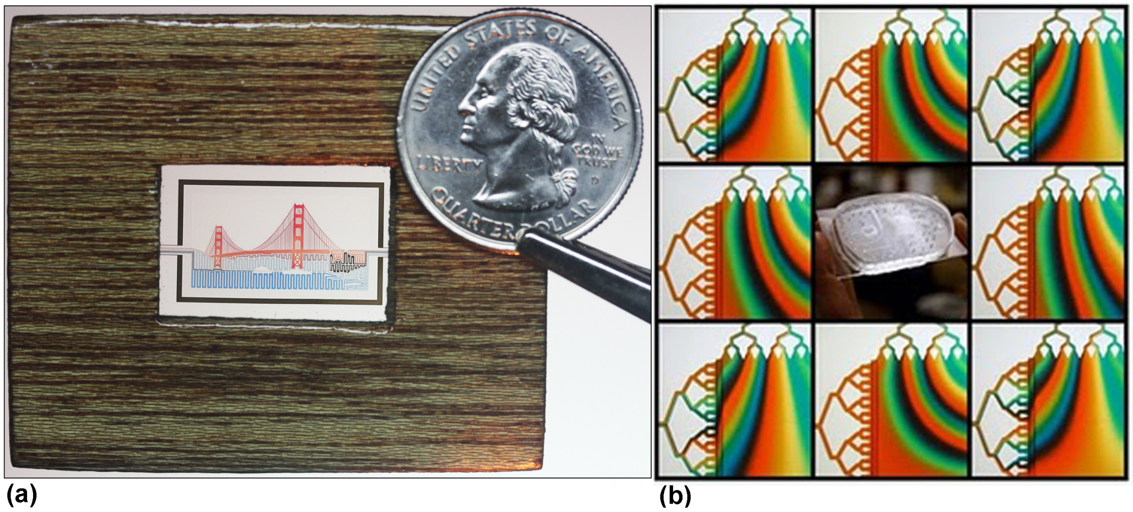

Figure 1: Examples of a microfluidic 'art' piece. (a) Courtesy of J. Tanner Navill, (b)'Gradient Festival' by Greg Cooksey and Albert Folch.

printers.

A great portion of the research in microfluidics has focused on fluid manipulation in the small scale. Having control over the fluid motion on the micro-scale provides an ability to create new methods for drug delivery [21], mixing efficiently, development of optofluidic elements [22–24], etc.

Controlled manipulation of highly viscous liquids can be extremely complicated due to the constant competition between inertial, viscous, capillary and body forces at large scale. As a consequence of these forces, highly viscous liquids experience coiling [25], viscous buckling [26], fingering [27] and folding [28]. Therefore, it is difficult to isolate one force and study its effect on the fluid motion.

Low-Reynolds-number flow is a flow where inertia forces play a very small part in the conditions which determine the fluid motions. The Reynolds number is a nondimensionalized number which compares inertial forces with the viscous ones and is defined as

$$Re = \frac{\rho V L}{\mu} \tag{1.1}$$

where $\rho$ is the fluid density, $V$ and $L$ are the characteristic velocity and length scale, respectively, and $\mu$ is the fluid viscosity. Reynolds number is a combination of three, quite disparate, physical quantities, hence, it can be observed in wide variety of physical phenomenon [29]. Few examples of these viscous dominated flows are: the bacteria movement, the motion of glaciers and the motion of highly viscous fluids such as tar, corresponding to a significantly small length scale $L$, characteristic $V$, and high viscosity $\mu$, respectively. Flows in microfluidics systems are mostly characterized as low-Reynolds-number flows, and investigating highly viscous liquids in small scale aggrandizes the effect of viscous forces.

To demonstrate the effect of viscous and capillary forces independently, we study the dynamics of two phase flow in microfluidic chambers. In small scale, the body forces can be completely neglected and surface forces are mainly dominant. We can reach high flow rates easily; only viscous and interfacial tension forces play a role in the flow morphology in a specific microchannel geometry. Furthermore, the sole influence of viscous forces can be investigated by conducting experiments with miscible liquids in regimes that the effect of molecular diffusion can be neglected.

Conducting experiments in small scale necessitates the use of microchannels as a tractable media. Therefore, there is a need to find new efficient techniques to fabricate micro-substrates. One of the most common methods of microfabrication is photolithography which has been perfected with the fabrication of semiconductors to create integrated circuits (IC). A great number of microfluidic channels are fabricated by photolithography, though there are other cheaper alternatives such as laser micromachining and PDMS based channels. This method is highly practiced mainly due to the capacity of these channels in maintaining high-pressure flows. However, complicated fabrication processes along with a higher cost and constraints on the topographies calls for other ideas.

In 1998, Xia and Whitesides [30] proposed soft lithography technique, which uses elastomers as the main material instead of expensive silicon wafers which are used in conventional photolithography, to overcome the challenges involved in the other lithography method. Nevertheless, even soft lithography has shortcomings such as fabricating channels with on average shorter lives and inability to resist high pressure/speed flows which makes it difficult to conduct experiments in a wide speed range.

Therefore, part of current investigation is dedicated to explore the potentials of $\mu$fabrication utilizing ultrafast lasers.

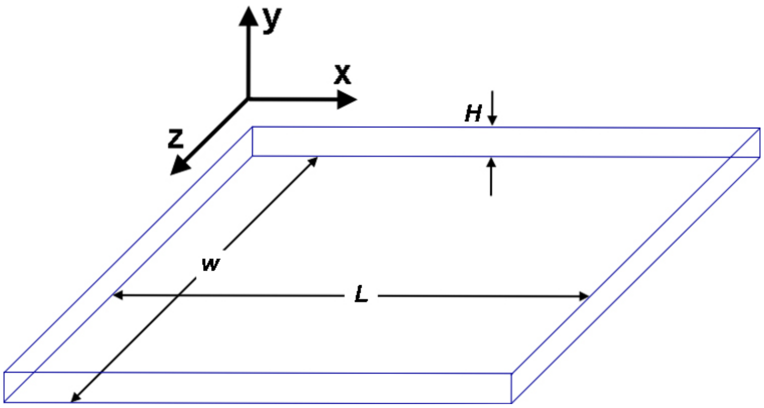

Figure 2: Example of a Hele-Shaw cell.

## 1.2 Theory of Viscous Core-Annular Flow

In the following sections, the highlights of the fluid dynamics theories involved in this study are discussed.

### 1.2.1 The Hele-Shaw cell

Two parallel plates with infinitesimally small gap is defined as the Hele-Shaw cell (Figure 2); in other words, the height to width ratio of the configuration must be significantly *small* in order to be able to use this approximation. There are many problems in fluid mechanics that deal with this kind of geometry, i.e. in oil fields when a viscous fluid fills the voids in a porous medium [31]. In microfluidics specifically, any planar configurations can be approximated with a Hele-Shaw cell.

The continuity and the full Navier-Stokes equations for any incompressible flow are as follows:

$$\nabla . V = 0 \tag{1.1}$$

$$\rho \frac{DV}{Dt} = f - \nabla P + \mu \nabla^2 V, \tag{1.2}$$

where V is the velocity vector, $\rho$ is the fluid density, $D$ is the substantial derivative, $f$ is the applied body forces, $P$ is the local pressure, and $\mu$ the fluid viscosity. However, applying the Hele-Shaw cell approximation $H/W << 1$ and $H/L << 1$, and the following scaling laws in $x, y$ and $z$ directions:

$$x \sim L, \quad y \sim H, \quad z \sim W$$

one can conclude that indeed the flow in the Hele-Shaw cell that is driven by a steady pressure can be considered two-dimensional (2D) and irrotational. Therefore, the advective terms ($V.\nabla$) are negligible compared to the viscous terms ($\mu\nabla^2 V$), and the governing equation becomes

$$\nabla P = \mu\nabla^2 V + f, \tag{1.3}$$

which is defined as Stokes flow (creeping flow). Given microfluidic circumstances, the body forces are negligible, therefore, the final governing equation is

$$\nabla P = \mu\nabla^2 u. \tag{1.4}$$

### 1.2.2 Potential Flow

The streamlines of the steady flow in the Hele-Shaw geometry are identical in shape with those in a hypothetical irrotational 2D flow of an inviscid fluid [32]. Any complex 2D incompressible inviscid flows can be built with a combination of these elementary flows: 1) uniform flow, 2) a source or sink, and 3) a vortex [33]. The flow inside the Hele-Shaw cell, with the same characteristics can also be generated with the superposition these basics flow.

Superposition of a source and a sink of equal strength separated by a distance $l$ can produce the flow in the Hele-Shaw cell far from the walls. The velocity components ($V_r$ and $V_\theta$), stream function ($\psi$) and the velocity potential ($\phi$) for a source flow are as follows:

$$V_r = \frac{q}{2\pi r}, \tag{1.5}$$

$$V_\theta = 0, \tag{1.6}$$

$$\psi = \frac{q}{2\pi}\theta, \tag{1.7}$$

$$\phi = \frac{q}{2\pi} lnr \tag{1.8}$$

where $q$ is the volume flow rate per unit depth.The same equations for a sink flow can be calculated by negating equations 1.5 through 1.8.

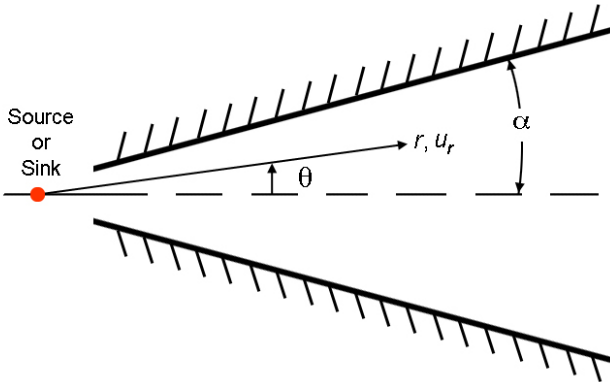

Figure 3: The configuration of Jeffery-Hamel flow.

### 1.2.3 Flow in Diverging or Converging Channels (*Jeffery-Hamel Flows*)

Consider two stationary plane walls separated by angle $-\alpha \leq \theta \leq \alpha$ (Figure 3). There is a 2D steady flow in the region between two walls generated by a source or a sink located at the intersection of the two walls. The flow in this configuration is named Jeffery-Hamel flow after two notable researchers who independently investigated the flow of incompressible viscous fluid in diverging and converging channels [32, 34–36]. The investigation continued more elaborately by Rosenhead in 1940 [37] and more recently Hayat *et all* applied the same theories for other kinds of fluids [36].

The governing equations for a Jeffery-Hamel flow can be expressed in polar coordinates (r,$\theta$). The continuity equation is

$$\frac{1}{r}\frac{\partial}{\partial r}(ru_r) = 0, \tag{1.9}$$

and assuming a purely radial flow ($u_\theta = 0$), the momentum equations are

$$u_r\frac{\partial u_r}{\partial r} = -\frac{1}{\rho}\frac{\partial p}{\partial r} + \nu(\frac{\partial^2 u_r}{\partial r^2} + \frac{1}{r}\frac{\partial u_r}{\partial r} - \frac{u_r}{r^2} + \frac{1}{r^2}\frac{\partial^2 u_r}{\partial \theta^2}), \tag{1.10}$$

$$0 = -\frac{1}{\rho}\frac{\partial p}{\partial \theta} + \frac{2\nu}{r^2}\frac{\partial u_r}{\partial \theta}, \tag{1.11}$$

where $r$ is the distance from the source (or sink), $\theta$ is the angle measured from the center line between the walls, $u_r$ and $u_\theta$ are the velocities in the $r$ and $\theta$ directions, respectively, $p$ is the fluid pressure, and $\rho$ and $\nu$ are the fluid density and kinematic viscosity, respectively. Equations 1.9 through 1.11 are solved with the similarity technique for solving partial

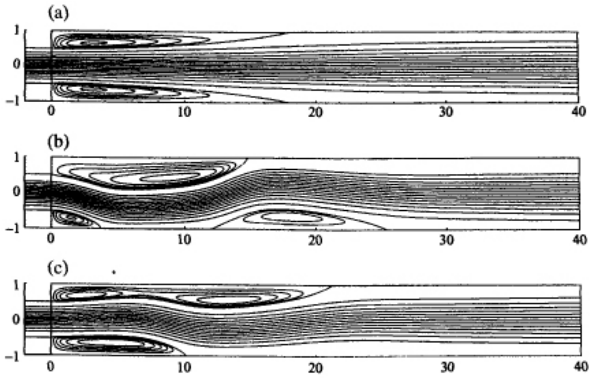

Figure 4: Numerical simulation of the flow in a diverging channel. (a) A symmetric flow (unstable). (b) An asymmetric flow. (c) Another asymmetric flow. [35]

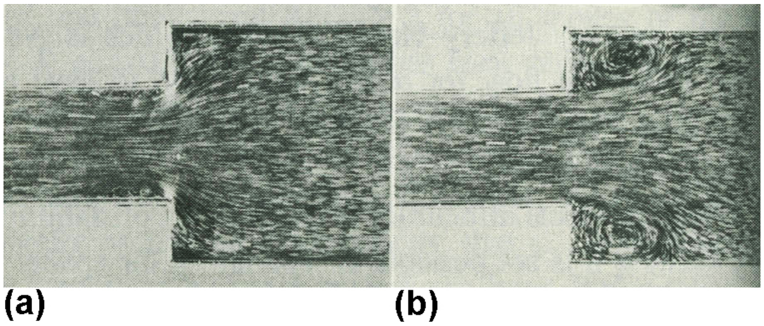

Figure 5: The flow in the diverging channel. (a) A low value of $Re$. (b) A five times higher value for $Re$. [35]

differential equations (PDEs) [34, 37]. The final solution of these PDEs is summarized as an elliptic integral which was investigated by Rosenhead and others under few physical circumstances to find the stable and unstable solutions for this specific kind of flow.

There are an infinite number of solutions for each $\alpha$ and Reynolds number ($Re = Ur\alpha/\nu$). Numerical and experimental results also show different regimes that the system can claim according to the mentioned parameters (Figure 4 and Figure 5). When the local value of $Re$ exceeds the critical Reynolds $Re_c$, purely divergent flow become impossible and a region of inflow may be expected to appear near one or both walls [32], similar to Figure 5 (b).

### 1.2.4 Core-Annular Flow

Two immiscible fluids have a tendency to arrange themselves in such a way that the low viscosity one is in the region of high shear to minimize the surface energies [38].

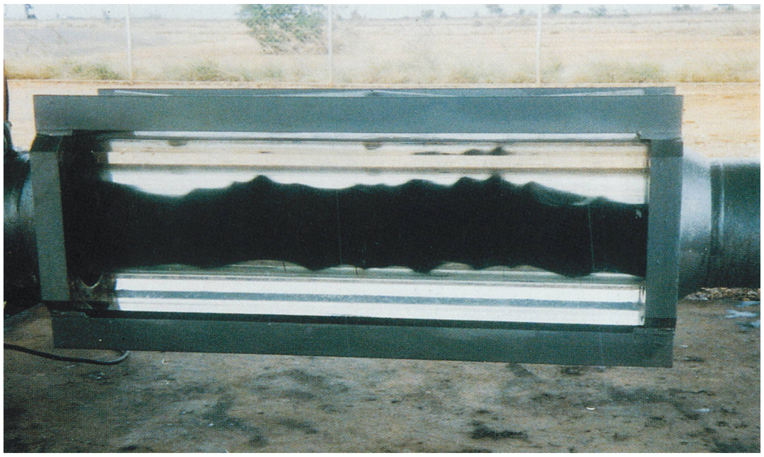

Figure 6: Core-annular flow of oil lubricated by water in a pipe of diameter 8” and test loop of length 1km at San Tome, Venezuela. [38]

This arrangement leads to a phenomenon called lubrication where the more viscous fluid is surrounded by the less viscous one. The co-flow of two liquids with one in the center of the other one is called core-annular flow. This effect has great applications in industries, i.e. lubrication of oil by water in transfer pipes (Figure 6).

Many properties of core-annular flow are vaguely understood from a theoretical point of view [38]. For instance, the interface between the two immiscible liquid can be unstable in some regimes. Also the flow rates directly effect the kind of regime the system attains. Hence, the two liquids can form an emulsion for high flow rates or a slug flow for low speeds. Another key factor in formation of core-annular flow is the role of interfacial tension between the two liquids. Therefore, it is particularly interesting to understand these factors in the formation of core-annular flows.

### 1.2.5 Saffman-Taylor Instability

Saffman-Taylor or Rayleigh-Taylor instability deals with the flow in a porous media. When two incompressible viscous fluids move in the vicinity of each other such that they share an interface, the fluid motion can undergo this kind of instability. For example, to drive oil from a reservoir usually some water is injected into the rocks. This leads to a phenomenon called viscous fingering. The first theory explaining this event was provided by Saffman and Taylor [31].

Figure 7: Example of Saffman-Taylor instability in a Hele-Shaw cell.[27]

### 1.2.6 Folding Instability

Viscous folding occurs in situations such as pouring honey on a piece of toast and formation of large-scale geological structures. It has been shown that folding instability happens in diverging microchannels [39] and the shape and evolution of folded viscous threads has also been studied [40]. The occurrence of this phenomenon is due to fluid's tendency in minimizing the viscous dissipation. For instance, when a lubricated viscous thread enters a diverging microchannel the extensional viscous stresses cause the thread to bend and fold, rather dilate [39].

### 1.2.7 Surface Tension

The origin of surface tension is rooted in the cohesive forces between molecules. Surface tension can be viewed as the work required to change the surface area of a volume of liquid. Imagine a rectangular wire frame with one of its sides replaced by a rod. Soaking this device in a bath of soap and water, a soap film can be captured in the frame. By pulling the rod, the area of the film increases and releasing it decreases the area. In a mathematical way, one can determine the change of area as below

$$\delta W = \gamma . dA, \tag{1.12}$$

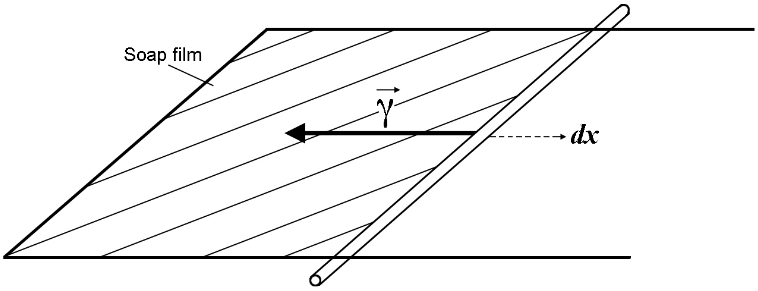

Figure 8: An experiment to show surface tension in terms of energy and force.

where $W$ is the work required to manipulate the area, which is equal and opposite in direction to the work done by surface tension, $A$ is the area, and finally $\gamma$ is the surface (interfacial) tension in units of $[J/m^2]$. Therefore, $\gamma$ can be interpreted as the energy required to change the area of a surface by one unit. In the same experiment $\gamma$ can be looked at as a force per unit length in the direction opposite of the rod motion

$$\delta F = \gamma . dx, \tag{1.13}$$

where $F$ is the force and $dx$ is the distance the rod moves.

### 1.2.8 Wetting and Dewetting

Wetting refers to the study of how a liquid is deposited on a solid or liquid substrate [20]. This physical phenomenon has many applications in various industries, for instance, in the chemical industry one of the key factors in determining a paint's quality is evaluating its ability to wet desired surfaces.

Generally, there are two types of wetting: total wetting and partial wetting. The type of wetting is evaluated by a spreading parameter $S$, which is the difference between the surface energy (per unit area) of the substrate when it is dry and wet:

$$S = E_{dry} - E_{wet}, \tag{1.14}$$

this formula can also be expressed in terms of surface tension

$$S = \gamma_{SO} - (\gamma_{SL} + \gamma), \tag{1.15}$$

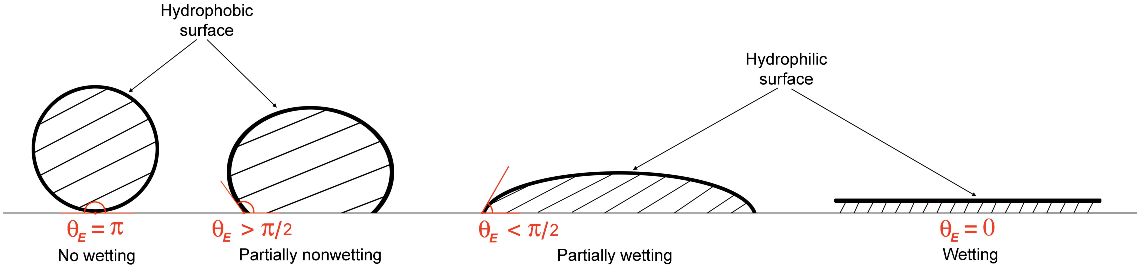

Figure 9: Different wetting regimes of a drop.

where $\gamma_{SO}$ is the surface tension at the solid/air, $\gamma_{SL}$ at solid/liquid and $\gamma$ at the liquid/air interfaces, respectively. In order to calculate $S$, one can use Young's relation

$$\gamma cos\theta_E = \gamma_{SO} - \gamma_{SL}. \tag{1.16}$$

Substituting 1.15 into 1.16 yields

$$S = \gamma(cos\theta_E - 1), \tag{1.17}$$

where $\theta_E$ is the contact angle between the liquid and the solid surface.

The type of wetting can be determined according to the sign of $S$. If $S > 0$, it is considered total wetting and if $S < 0$, partial wetting. Another classification which is based on $\theta_E$, defines a surface to be hydrophobic and partially nonwetting when $\theta_E > \pi/2$ and hydrophilic and partially wetting when $\theta_E \leq \pi/2$ (Figure 9). The two extreme cases where $\theta_E = 0$ and $\theta_E = \pi$ refer to total wetting and no wetting regimes, respectively. In addition, the wetting of a liquid on a solid surface in air is a well known phenomenon [41]. By contrast, the wetting behavior of liquid dispersion (liquid/liquid) flowing in microgeometries is relatively less understood[42].

# 2 Microchannel Fabrication

All the experiments for current investigation were conducted in microchannels fabricated with conventional photolithography technique. However, in an effort to produce microchannels with both cost efficiency and resistance to high pressure flows for future experiments, laser micromachining have been explored.

In order to be able to use lasers for etching on different materials it is important to know how the laser effects these materials. In other words, there needs to be a calibration of the laser based on its parameters such as power and speed that allows for planning the fabrication of a specific piece with certain dimensions.

Three different materials were used for laser calibration: borosilicate glass, soda-lime glass and PDMS elastomer. On each piece trenches were ablated with a Gaussian beam of a femtosecond laser. The number of passes, and the power used for etching were varied for each trench. Optical microscopy is then used to record the shape of each trench. In addition, the minimum essential power for ablation (threshold power) was found for each material and the effect of increasing the power on the geometry of the channel is reported. Ultimately, the height of each trench on different materials is shown as a function of a nondimensional number which corresponds to the laser pulses per channel width.

## 2.1 Photolithography Technique

Photolithography, the most common form of lithography, is widely used in microfabrication. Lithography itself is derived from two Greek words: [lithos] and [graphein] which mean stone and to write, respectively [43]. Basically, any lithography refers to writing or printing of a pattern on a solid surface; i.e. silicon wafer.

Every photolithography fabrication is done in a cleanroom and can consist of few post-exposure treatments and/or slightly different baking processes but almost all of them follow the same procedures. The common steps in manufacturing a microchannel utilizing the photolithography method are as follow: cleaning the substrate, adding the photoresist (PR), UV exposure, developing, hard baking and etching.

Cleaning the substrate (i.e. silicon wafer) and removing all possible contaminations off of the surface is important in making a microchannel. Usually a layer of silicon oxide is added to prevent possible destruction of the solid surface during any etching processes. Then a layer of photoresist is uniformly dispersed on the surface with a spinner to a specific height according to the final application of the piece. Sometimes soft baking of the substrate is necessary to reduce the residual stress from spinning and vaporizing the extra moisture out of the solvent.

The PR type, either negative or positive, determines the outcome of the UV exposure process. Basically, UV light is responsible for chemically changing the PR. The exposed positive PR becomes more soluble in the developer solution while the negative one becomes polymerized and is not removed by the developer. Over all, in microfabrication positive PR is mostly used.

Similar to photography, there needs to be a developing procedure to form the image on the surface. Development is essentially dissolving PR selectively which can be done either as a wet or dry process [43]. Finally, to prepare the substrate for etching there is a hard-baking step left to finish the fabrication procedure. This treatment guarantees a hard film while removing the residual developing solvents and renders an adequate adhesion of the PR. Sometimes, in order to prolong the life of the resist the hard-baking must be repeated.

Successfully finishing the previous steps provides a proper platform for etching the desired channel geometry on the treated wafer with any available etching methods such as dry etching.

## 2.2 Laser micromachining

Laser $\mu$machining is another method used for microchannel fabrication. One of the main advantages of implementing lasers in fabrication of micro scale structures is the ability of these devices in functioning under ambient conditions and at room temperatures. Therefore, this method eliminates the need for expensive clean room facilities, as well as any post processing procedures once the desired geometry is etched. However, like any

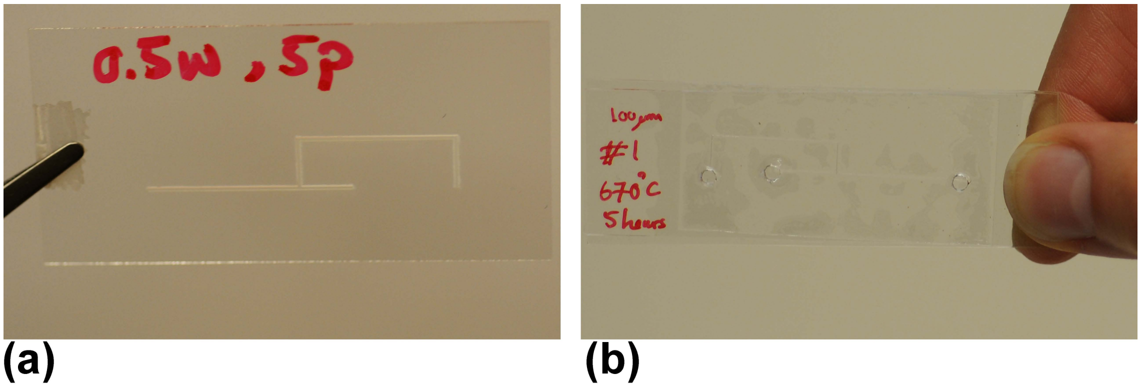

Figure 10: (a) A soda-lime glass etched through with a simple geometry. (b) Microchannel after fusion boding in a furnace for 10 hours.

other method it has a few disadvantages such as the high initial cost of laser, optics and motion system; high maintenance costs, and the need for more highly skilled operators to perform the fabrication processes.

To test the idea of fabrication of microchannels with ultrafast lasers, we etched the entire thickness (150$\mu$m) of a soda-lime glass slide (manufactured by *J. Melvin Freed Brand*) with a simple two-inlet microchannel geometry (Figure 10 (a)). Then the piece of glass with the channel layout engraved on it was cleaned and sandwiched between two other soda-lime glass slides with thickness 100$\mu$m. The top glass was drilled with three holes, two for fluid inlet and one for outlet. Finally, the glass module was put in a furnace for 10 hours at constant temperature 600 degree Celsius for fusion bonding of glass pieces. The plastic fittings were then glued on the inlets and outlet. The microchannel was tested with water and oil (Figure 10). The experiment was run for about an hour and there was no evidence of leaking in the channel.

## 2.3 Laser Calibration

### 2.3.1 Experimental Procedure

The experimental setup for laser micromachining of glass and PDMS substrates is shown in Figure 12. A Spectra-Physics *SpitFire Pro* amplified femtosecond laser was used for all micromachining processes. This laser system has a nominal wavelength $\lambda = 800$ nm, a repetition rate $f = 1000$ Hz, a nominal pulse duration of 120 fs, and a maximum

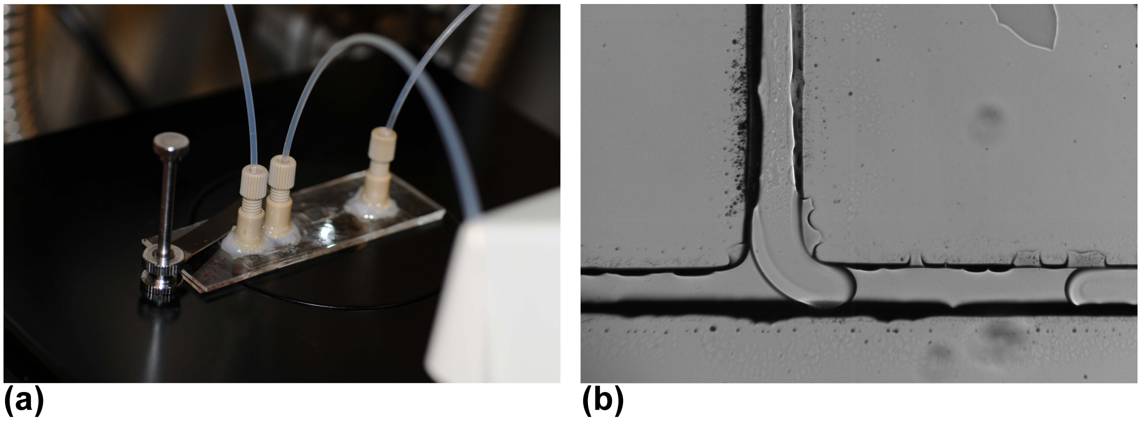

Figure 11: (a) Microchannel shown in an experiment on an inverted microscope. (b) Experimental picture water/oil fluid pair in the microchannel fabricated with ultrafast laser $\mu$machining.

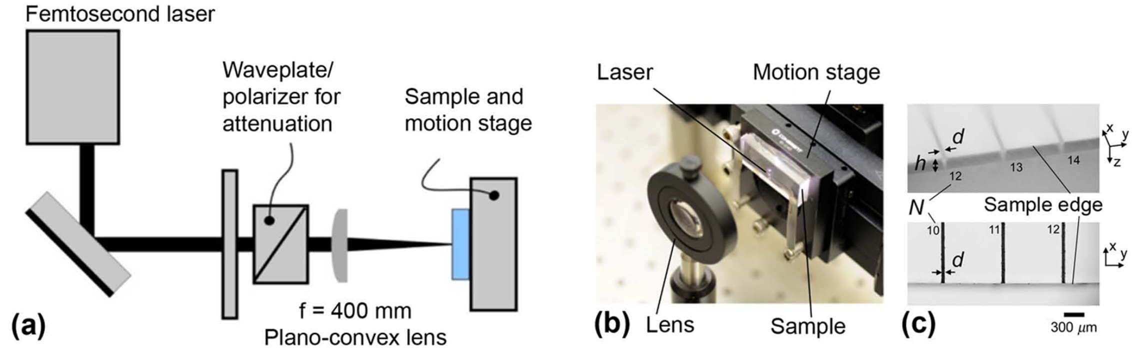

Figure 12: (a) Schematic of experimental setup for laser ablation. (b) Photograph taken dusring the processing of a slab of PDMS elastomer. (c) Micromachined trenches with different number of passes $N$.

energy of 2.1 mJ/pulse. The beam is horizontally polarized upon exiting the laser, and the mode shape is nearly $TEM_{00}$ with $M^2 = 1.3$. The polarizer sends a specific portion of the wave through the lens according to the selected power. The lens is a quartz plano-convex unit with a focal length of $f_L = 400$ mm. All sample pieces are located at the focal point which is found in the darkened room by locating the brightest spot when a piece of paper is moved in the range in which the focal point is expected to be. Each time a sample is located on the stage, necessary adjustment should be done to place the surface of the test piece exactly at the focal point.

We used three materials for calibrating the laser: borosilicate and soda-lime glass, and PDMS elastomer. PDMS pieces were made out of a silicon elastomer kit manufac-

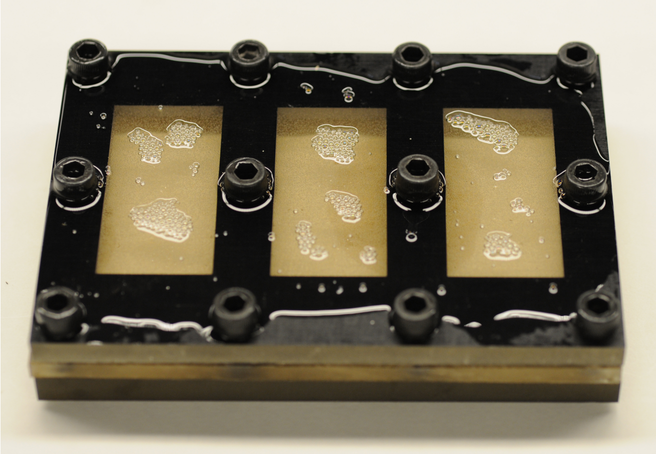

Figure 13: The mold used to make PDMS pieces for laser micromachining.

tured by *Down Corning Sylgard 184*. The kit contains liquid PDMS and a cross linker. These two liquids were mixed with a 10 to 1 weight ratio. The combination was stirred vigorously and then poured into a mold (Figure 13). The mix solidifies in 24 hours, however, in order to avoid the sticky surfaces the samples are removed out of the mold after 48 hours.

For each ablation test, the sample is located at the focal point on a 3-axis linear positioning system (Coherent LabMotion) that moves the sample as needed and also controls the laser beam delivery. In order to make sure that the ablated material has a place to escape and the machining starts form outside and moves towards the sample piece.

To find a correlation between the laser power and the degree of ablation, we used a program as follows: on every sample 16 trenches that are 1 mm apart are made. Each trench is a succession of multiple laser paths based on the number of the trench. For instance, the first trench is one path, the second one is two paths and on the Nth trench the laser has ablated N times with the velocity $V$.

After the laser ablation, each sample is located vertically on an inverted microscope. The piece is illuminated with a fiber optic bundle which emits light on top of the targeted trench. Then a photograph of each trench is taken with the appropriate zooming of the microscope. These images are then used for analyzing the trench's geometry based on the power, velocity and the number of passes.

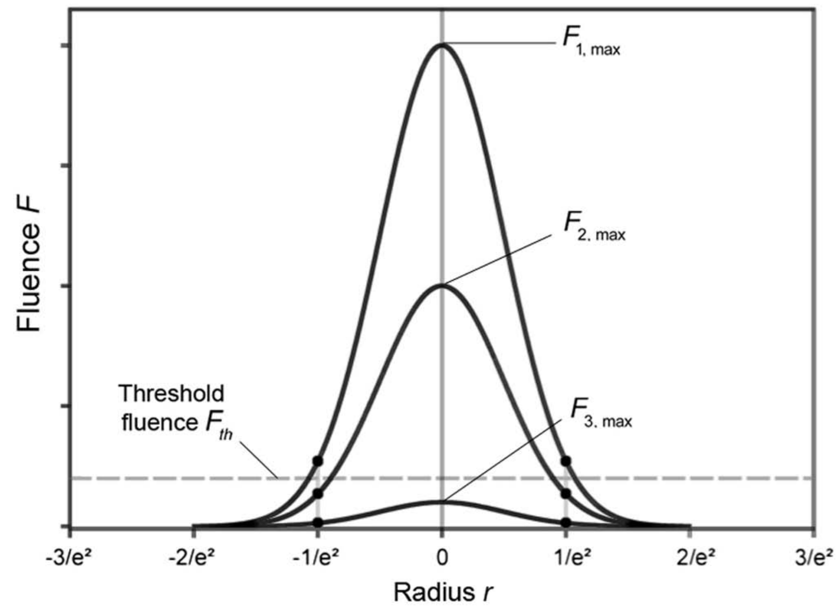

Figure 14: Gaussian pulse profile and example of threshold fluence, $F_{th}$.

### 2.3.2 Laser Beam Diameter

The laser beam fluence has a Gaussian distribution as follows [44]:

$$F(r) = F_{max}exp(\frac{-2r^2}{a^2}), \tag{2.1}$$

where $r$ is the radial distance from the beam centerline, and $F_{max}$ is the maximum fluence (at $r = 0$). The optical beam radius $a$ is defined to be the $r$ when the fluence is $1/e^2.F_{max}$, which is the same for all laser peak fluences (Figure 14). In addition, for a laser to start ablation the fluence has to be at least equal to the threshold fluence $F_{th}$. For instance, $F_1$ and $F_2$ will produce channels however, $F_3$ will not produce channels at all. Therefore, condition for material removal is $F \geq F_{th}$.

Using 2.1, the channel diameter can be determined as the $r$ for which material will be removed

$$r = a(0.5ln(\frac{F_{max}}{F_{th}}))^{0.5}. \tag{2.2}$$

Since the incident beam diameter $d_i = 2a$ is defined as the diameter when the fluence drops to $1/e^2.F_{max} \approx F_{max}/7$, one would expect the channel width to be on the order of the beam diameter, i.e., $d \sim d_i$ when $F_{max} \sim 7F_{th}$.

### 2.3.3 Results

The channel width $d$ and height $h$ of every trench were systematically measured from the photographs. Defining the channel aspect ratio as $\alpha = h/d$, a correlation between the system parameters, laser speed $V$, power $P$, pulse frequency $f$, and $N$, with the geometrical parameters can be concluded. As it is shown in Figure 15 (a), d increases with the channel aspect ratio for $\alpha < 2$ and remains relatively constant at a final diameter $d_f$ for $\alpha > 2$. The final diameter $d_f$ is also a function of the incident laser power $P$ (Figure 15 (b)). The threshold power $P_{th}$ for borosilicate glass, soda-lime glass and PDMS elastomer were recorded as 95, 75 and 55mW, corresponding to threshold fluence $F_{th} = 2.0$, 1.8 and 1.2 $[J/m^2]$, respectively which were determined as below:

$$F_{th} = \frac{2P_{th}}{\pi f a^2}. \tag{2.3}$$

Figure 15 (c), indicates that for both glass materials, indeed, $d \sim d_i$ when $F_{max} \sim 7F_{th}$ as was predicted before. However, for the PDMS elastomer when $F_{max} \sim 7F_{th}$ the measured $d$ is several times greater than the predicted values. This difference is due to the flexible characteristics of this kind of material and the specific way it behaves under laser ablation. Further investigation is needed to fully determine the mechanism of ablation and key parameters for this type of material.

Another way to predict the final channel diameter is to fit the data on $d_f/d_i$ vs. $F_{max}/F_{th}$ using

$$d_f/d_i = \kappa(ln(\frac{F_{max}}{F_{th}}))^{0.5}, \tag{2.4}$$

where it provides $\kappa = 0.88, 0.85$, and 1.65 for borosilicate, soda-lime, and PDMS substrates, respectively.

In order to determine the effect of $N$ on $h$, other system parameters (velocity, power and material) were kept constant. The edges of trenches were extracted from each photograph and superimposed on each other (Figure 16). The superposition indicates that the channel width $d$ reaches a plateau $d_f$ after $N \approx 2 - 3$ when $\alpha > 2$. This effect can also be traced in Figure 15 (a). Looking closely at the channel profiles, $h$ increases with $N$ more drastically than $d$ does. Interestingly enough, the geometry of trenches made in

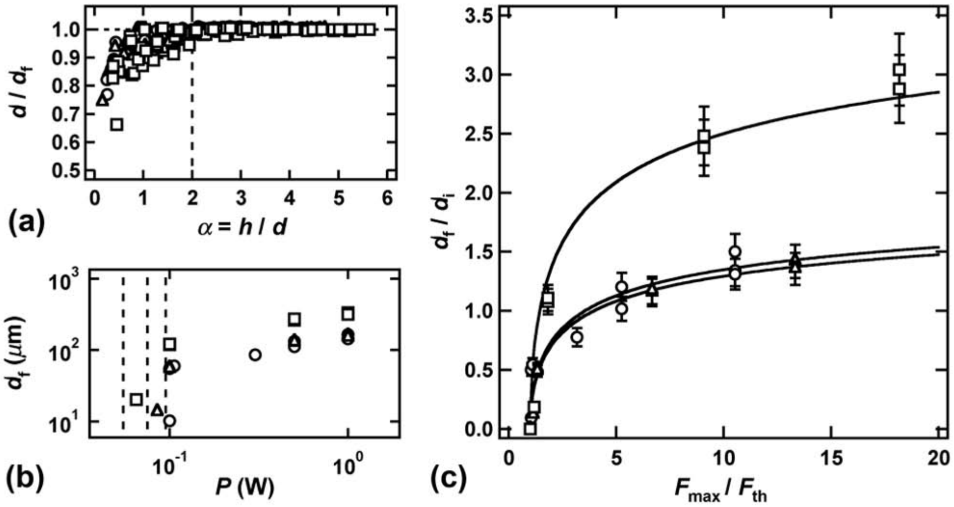

Figure 15: Evolution of channel width $d$. Materials: borosilicate glass (○), soda-lime glass (△), PDMS elastomer (□). (a) Influence of the channel aspect ratio $\alpha = h/d$. (b) Final channel width $d_f$ vs. incident laser power. Dashed-lines: threshold of ablation process. (c) Evolution of the final channel width $d_f$ scaled by the incident laser beam diameter $d_i$ as a function of the ratio of the maximum fluence $F_{max}$ to the threshold fluence $F_{th}$. Solid lines: $d_f/d_i = \kappa(ln(F_{max}/F_{th}))^{0.5}$ with $\kappa = 0.88$ (borosilicate), 0.85 (soda-lime), and 1.65 (PDMS).

both glasses have a ”V” type topography and look very similar to a Gaussian distribution. In other words, the laser beam leaves its intensity footprints graved into the glass. In contrast, the trench geometry in the PDMS is more rounded at the end and the edges are not as sharp as in the other two materials which is directly related to the flexibility of this specific material.

As a final analysis on the ablation of three test materials, the height $h$ of each trench was related to a nondimensional parameter $\Omega$ which contains all the system parameters as below

$$\Omega = \frac{Ndf}{V}, \tag{2.5}$$

where $d$ is the effective channel diameter measured from the photographs, $N$ is number of passes (ranging between 1 to 16), and laser frequency, $f = 1000$ Hz. This parameter is basically the number of pulses per channel diameter. Rescaling all the measured heights with $\Omega$ leads to a single curve (Figure 17) for channels with aspect ratios varying between

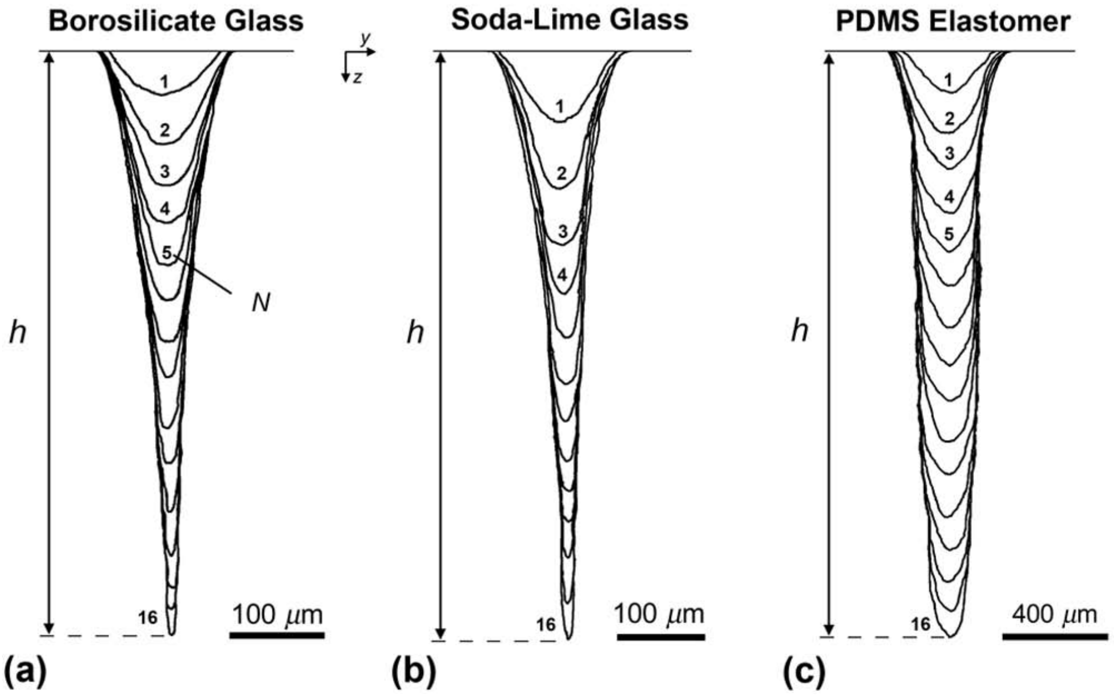

Figure 16: Influence of the number of passes $N$ on microtrenches profiles: (a) borosilicate glass, (b) soda-lime glass, and (c) PDMS elastomer.

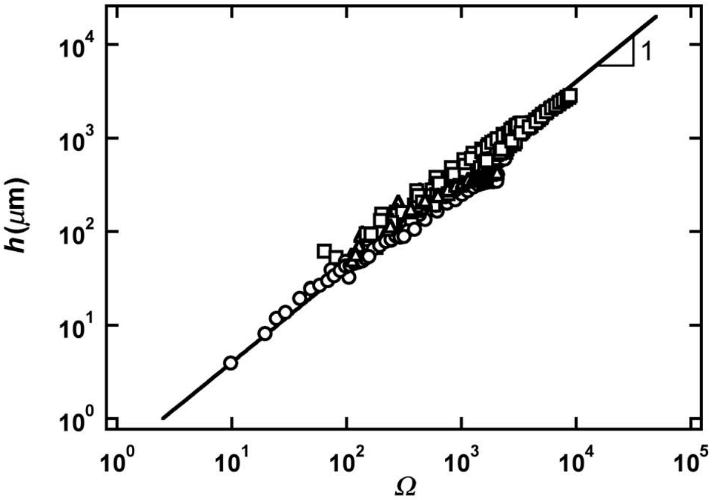

Figure 17: Evolution of the channel height $h$ versus number of laser pulses per channel width $\Omega = Ndf/V$ with materials: borosilicate glass (○), soda-lime glass (△), and PDMS elastomer (□). Low and large aspect ratios (i.e., $\alpha < 1$ and $\alpha > 12$) and are not displayed. Solid line: $h = 0.4\Omega$.

1 to 12. The curve is fit with the function

$$h = c\Omega, \tag{2.6}$$

where $c = 0.4\ \mu$m/pulse. For $\alpha > 15$, the curve overestimates the ablation penetration depth $h$ into the material, as in practice $h$ asymptotically reaches a plateau around $\alpha \approx 15$.

# 3 Experimental Procedures

Generally microfluidic experiments share a number of essential elements as follows: microchannels, microscopy with appropriate illumination, image acquisition, and fluids. However, methods by which microchannels are fabricated, the kind of microscopy and data collection techniques, and the choice of fluids can very greatly. For instance, the selected fabrication method for a microchannel depends strongly on its application; usually for high pressure flows photolithographically fabricated channels are used.

Specifically, in the current investigation, in order to explore viscous core-annular flow, we used microchannels with different geometries, a high speed camera, a fiber optic light for illumination, glass syringes and syringe pumps, PDMS with various viscosities, and some other alcohols. The detail of the equipments along with the experimental setup are explained in the following sections.

## 3.1 Experimental Setup

### 3.1.1 Microfluidic System

Microfluidic modules made out of silicon and glass were fabricated with the classical photolithography technique that was discussed in the preceding chapter. The thickness $h$, of the double-sided silicon wafers that were used in fabrication of these channels is 100 or 250 $\mu$m. Each glass/silicon/glass sandwich structure consists of three inlets and one outlet, a hydrodynamic focusing section (t-section), a square channel, and a diverging-converging chamber which can be modeled as a Hele-Shaw cell (Figure 18).

The hydrodynamic focusing section is a great tool to produce a viscous thread out of the injected liquids (the thread formation process will be discussed in later sections). Also, the square channel provides enough time for the thread to stabilize itself. For these experiments the microchannel has a square shape chamber following the hydrodynamic section and the square channel (Figure 18).

These hard microchannels provide an excellent platform to investigate high-pressure flow without deformation. Their chemical resistance is another advantage of using anodically bonded microchannels.

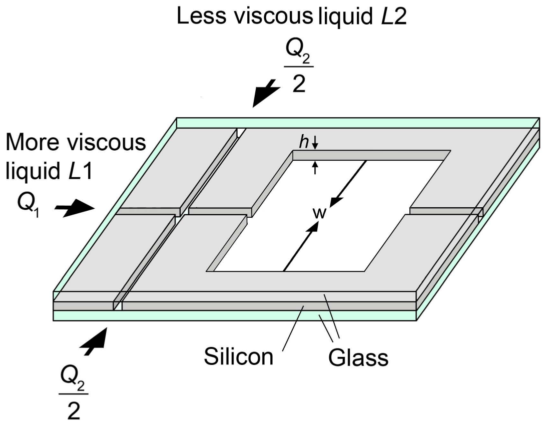

Figure 18: Microchannel layout with square chamber.

| Equipment | Company | Model |
|---|---|---|
| High-speed camera | *REDLAKE* | MotionXtra HG-100K |
| Microscope | Accu-Scope | 3035 |
| Light | *Fiber-Lite* | MI-150 |
| Syringe pump | *New Era Pump Systems, Inc.* | NE-1010 |
| Syringe | Hamilton | 1000 Series |

Table 1: Experimental equipment.

### 3.1.2 Other Equipment

As shown in Figure 19, the microchannel is placed on the stage of an inverted microscope with 5x, 10x and 20x lenses. The microscope is equipped with a trinocular head for mounting cameras. A high speed camera capable of recording from 1000 frames per second at full resolution, to 100000 frames per second at reduced resolutions is used for high speed imaging. In order to provide illumination, a fiber light bundle is mounted such that it lightens selected parts of the channel, and the flexible stage of the microscope makes it possible to move the channel for investigating specific areas. To control the flow rates, three syringe pumps are connected to the inlets of microchannel and can introduce the liquid with a desired flow rate into the channel. Having control on these flow rates is a key factor in the thread formation process. The detail of each equipment along with the name of the manufacturer is provided in table 1.

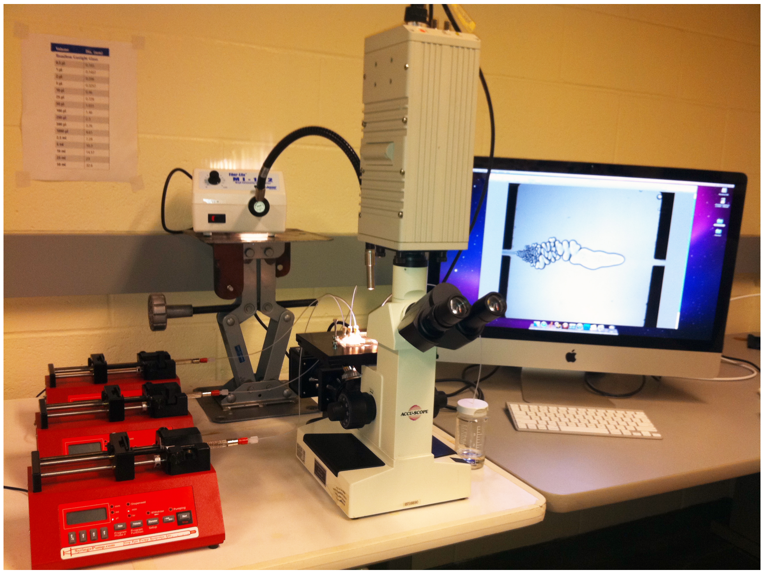

Figure 19: Experimental apparatus.

### 3.1.3 Fluids

Polydimethylsiloxane (PDMS) oils with a wide range of viscosity: $0.82 < \eta < 4865$ cP, is used to study the miscible core-annular flow. These polymeric oils are fully miscible and considered Newtonian in the range of shear rates $\gamma$ investigated in these experiments ($\gamma < 10^3 s^{-1}$). PDMS is a simple and well characterized test liquid, and unlike many other fluids it has a wide functional temperature range without a significant change in its viscosity. Other characteristics of PDMS that make it conveniently applicable for experiments are: shear stability, dielectric stability, high compressibility, chemical inertness, low surface tension, and low toxicity.

To study the immiscible core-annular flow, PDMS is paired with ethanol ($\eta = 1.16$ cP). Ethanol is the basic alcohol fuel produced from biomass. It is also used abundantly in the food and beverage industries. The technological aspects of these two fluids and their viscosities and surface tensions are the key factors in selecting fluids for these experiments. Overall, the important factor in choosing fluids for the current experiments is to select newtonian liquids which have well characterize behavior.

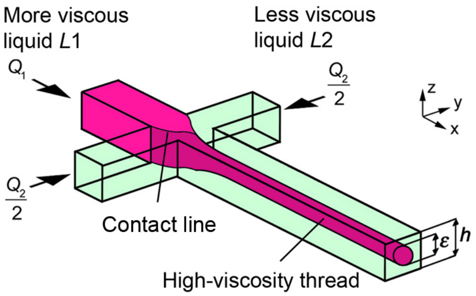

Figure 20: Formation of a highly viscous thread in a hydrodynamic focusing section. [45]

## 3.2 Thread Formation

The microchannels used to study viscous core-annular flow consist of a hydrodynamic focusing section which is responsible for thread formation (Figure 20). The more viscous liquid ($L1$) with a viscosity of $\eta_1$ and a flow rate of $Q_1$ is introduced in the center as the core fluid. Similarly, the less viscous liquid ($L2$) with a total flow rate of $Q_2$ and a viscosity of $\eta_2$ is injected symmetrically in the side channels. Hence, a viscous thread, lubricated by the less viscous liquid, is formed in the square channel upon meeting of the fluid pair at the T-section. The literature study suggests that given a viscosity contrast $\chi > 15$, the formation of a lubricated thread is guaranteed [45]. This thread formation method provides a great tool to study a viscous thread closely. Besides, the significance of this thread formation technique is the fact that the size of a thread in the square channel solely changes with the flow rate ratio and does not depend on the fluid properties [39, 45, 46].

## 3.3 Thread Size

Previous studies have shown that the thread size is independent of the fluid properties and can be manipulated only by changing the flow rates (Figure 21) [39, 45, 46]. The thread size $\varepsilon$ normalized by the channel height $h$ has found to be

$$\frac{\varepsilon}{h} = (\frac{\varphi}{2})^{0.5}. \tag{3.1}$$

Equation 3.1 is valid for both miscible and immiscible fluid pairs taking into ac-

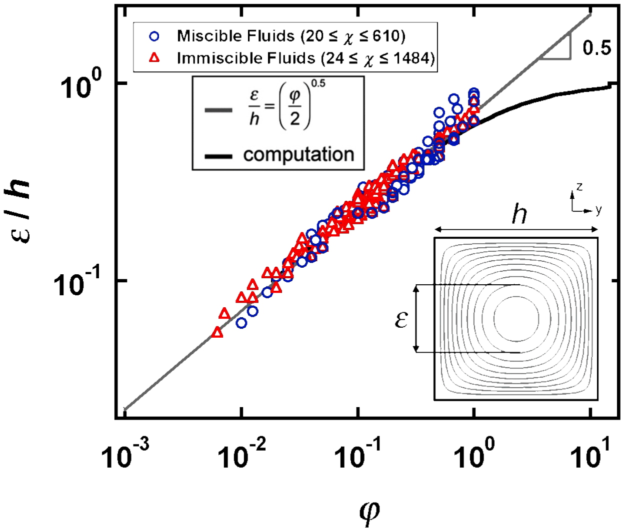

Figure 21: Evolution of core diameter $\varepsilon/h$ versus flow rate ratio $\varphi$ for a thread in plug flow in a square microchannel. Inset: cross-sectional contour plot of a set of iso-velocity contours in a square duct calculated using Fourier analysis.
[39, 45, 46]

count a limit for each one. In the former case where there is a chance of mixing eventually affecting the thread size, in order to be able to use 3.1 scaling law, the Peclet number should be $Pe > 10^3$. Peclet number is a nondimensionalized number that compares convection with diffusion effects and usually is defined as follows:

$$Pe = \frac{hV}{D} \tag{3.2}$$

where $V$ is the average flow velocity, $D$ is the molecular diffusion coefficient and $h$ is the channel height. In other words, if convection effects are 1000 times greater in magnitude than the molecular dissipation between the two liquids, molecular diffusion can be considered negligible.

For the latter case, where the interfacial tension forces play an important role in the flow behavior, applying 3.1 is confined by the capillary number $Ca_1 > 10^{-1}$. $Ca_1$ is the capillary number associated with the injected flow rate of the more viscous liquid and is defined as below

$$Ca_1 = \frac{\eta_1 Q_1}{\gamma_{12} h^2} \tag{3.3}$$

where $\gamma_{12}$ is the interfacial tension between $L1$ and $L2$. Capillary number, another nondimensionalized number, is the ratio of viscous and interfacial tension forces.

# 4 Results and Discussions

In this chapter, the experimental results of the behavior of miscible threads are first presented to shed light on the effect of viscosity without the complication involved with capillary effects. Analyzing the flow morphologies in the square chamber for various viscosity ratios indicates when lubrication failure occurs for various liquid pairs. Then the behavior of non-wetting capillary threads are shown and compared with studies on partial wetting threads.

## 4.1 Single Phase Flow

The flow behavior in the microchannels shown in figure 18 can be analyzed with a Hele-Shaw approximation [47]. In such cells, the flow is irrotational and the streamlines are expected to be identical to an inviscid fluid in a steady flow [32]. The single phase flow in the microchamber provides an insight for further investigating the multiphase flow; in other words it is a flow with viscosity contrast $\chi = 1$ and the results from other viscosity contrasts can be compared with this simple model.

In order to study the behavior of a single phase flow in a microchannel, the flow was seeded with 2 $\mu$m diameter spheres. The consecutive recorded images by the speed camera were superimposed on top of one another with IMAGEJ software to capture the streamlines entering the chamber through the inlet and exiting through the outlet. Similar to superposition of elementary plane flows [48], the inlet and outlet flow can be modeled as a source and sink flow, respectively, with equal strength and separated with a distance equal to the channel width $w$. Figure 22(a) shows streamlines that can be approximated by circular arcs which are identifiable with the angle they enter the chamber $\alpha$, hence the equipotential lines that are perpendicular to the streamlines are also circular. Furthermore, the potential flow approach suggests that the mean flow velocity in the first section of the chamber changes as follows:

$$V \propto \frac{1}{r}. \tag{4.1}$$

A similar effect is observed in a multiphase flow, where threads follow arc of circles upon

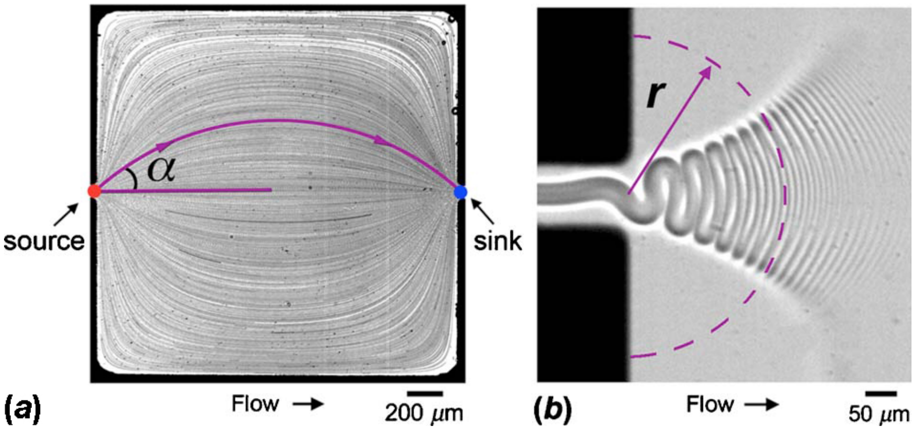

Figure 22: (*a*) Single-phase flow streamlines, and (*b*) folding morphology at the chamber inlet.

entering the chamber (Figure 22(b)).

## 4.2 Miscible Core-Annular flow

Studying miscible core-annular flow, provided that the Peclet number is large enough ($Pe > 10^3$), is an effective way to separately investigate the influence of viscosity contrast without complications involved with surface tension forces. Later on, these results can be compared with the immiscible case, considering the fact that in both cases the initial conditions (thread size $\varepsilon$) are the same, due to the fact that thread sizes only depend on the flow rate ratio (3.1) and not on the viscosity contrast $\chi$ or interfacial tension $\gamma_{12}$.

Initially, miscible viscous threads are formed in the hydrodynamic focusing section. Downstream, threads start folding upon entering the diverging section of the chamber and define an envelope that typically increases in amplitude $A$. The envelope size $A$ decreases in the second section prior to exiting the chamber (Figure 23(b),(c)). There are two possible scenarios for every thread in the chamber: (1) small threads that can traverse the chamber while being lubricated by $L2$ at the top and bottom walls and (2) large threads that make direct contact with the top and bottom walls. We define the latter, where the thread lubrication fails, 'piling' regime. This is due to the pile of $L1$ in the central region of the chamber that is touching the walls, and is similar to parallel viscous flows [49]. The former case is defined as the 'threading' regime because the initial thread is always

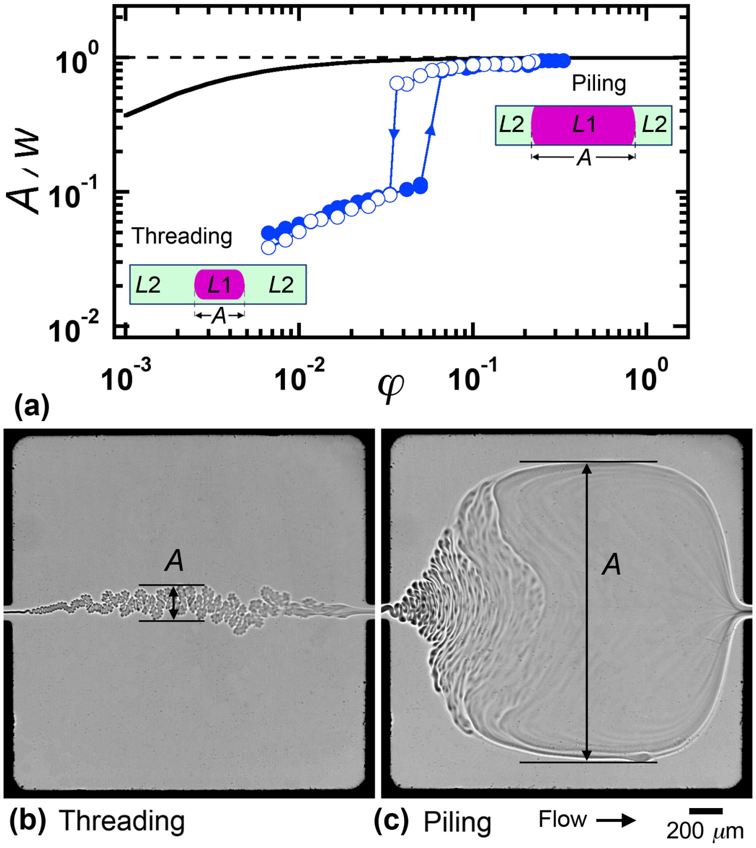

Figure 23: Lubrication failure of a viscous thread for $\chi = 592$. (*a*) Hysteresis loop between threading and piling regimes: increasing $\varphi$ (●) and decreasing $\varphi$ (○). Solid line: $A/w = [1 + (\chi\varphi)^{-1}]^{-1}$. Experimental pictures with flow rates ($\mu$ ml/min): (*b*) $Q_1 = 2$, $Q_2 = 110$, and (*c*) $Q_1 = 5$, $Q_2 = 40$

lubricated inside the chamber and attains the same status even before exiting the chamber.

One way to determine the system's regime is to examine the size of the envelope amplitude. The measured average envelope amplitude $A$ normalized by the channel width $A/w$ can be defined as a function of the flow rate ratio $\varphi = Q_1/Q_2$ (Figure 23(a)). Every thread, based on its viscosity contrast and flow rate ratio in a specific channel geometry, can be either in the piling or the threading regime. However, the transition between these regimes is not only based on the viscosity contrast $\chi$ and the flow rate ratios $\varphi$ but also on the history of the system. We have investigated the hysteresis in the transition by comparing the envelope amplitude A between a system initially in the threading regime and increasing $\varphi$ (i.e., increasing the initial thread diameter $\varepsilon$) with a system initially in the piling regime and decreasing $\varphi$ (i.e., decreasing $\varepsilon$). Data show that near the transition

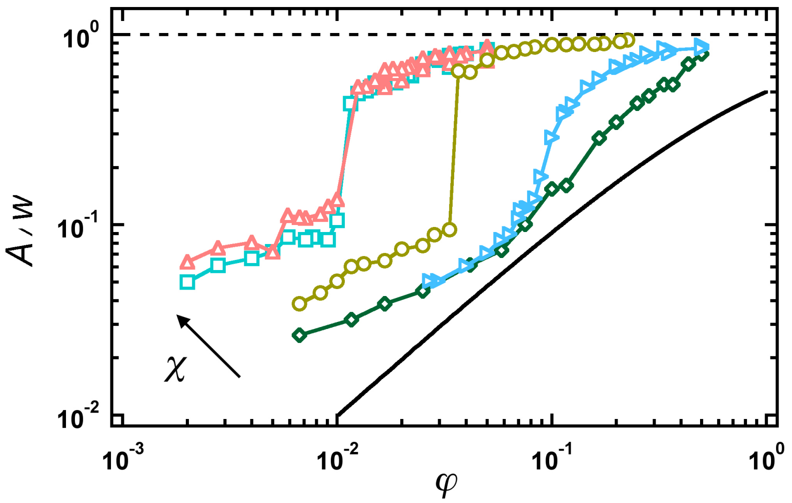

Figure 24: Evolution of the amplitude $A$ for $\chi = 52(\diamond)$, $\chi = 106(\triangleright)$, $\chi = 592(\circ)$, $\chi = 2796(\square)$, and $\chi = 5933(\triangle)$. Solid line: $A/w = [1 + \varphi^{-1}]^{-1}$.

the system can choose different configurations while in the well-defined threading and piling regimes, hysteresis is negligible.

Since the piling regime can be approximated with a parallel viscous flow, in Figure 23(a), the expected viscous parallel flow approximation is plotted (solid black line). This approximation is defined as below [49]

$$\frac{A}{w} = (1 + (\chi\varphi)^{-1})^{-1}, \tag{4.2}$$

and asymptotically matches data for large $A$. Overall, hysteric effects can alter the critical flow rate ratio $\varphi_c$ for the thread lubrication failure by a factor two. This uncertainty in the transition, however, is relatively small compared to the range of variation of $\varphi$ that spans over two orders of magnitude.

To cover a wide viscosity contrast range, similar experiments were conducted to investigate the effect of viscosity ratio $\chi$ on the lubrication failure (Figure 24). Focus is given to the behavior of weakly diffusive threads, data are only shown for cases where flow rate ratio decreases and the Peclet number is large ($Pe > 10^3$). For small viscosity ratios, the transition between the two regimes is smooth and occurs at a larger flow rate ratio $\varphi$.

As the viscosity ratio increases there is an abrupt variation in the amplitude $A$. This behavior is related to the ability of a thread to bend in a viscous environment. In

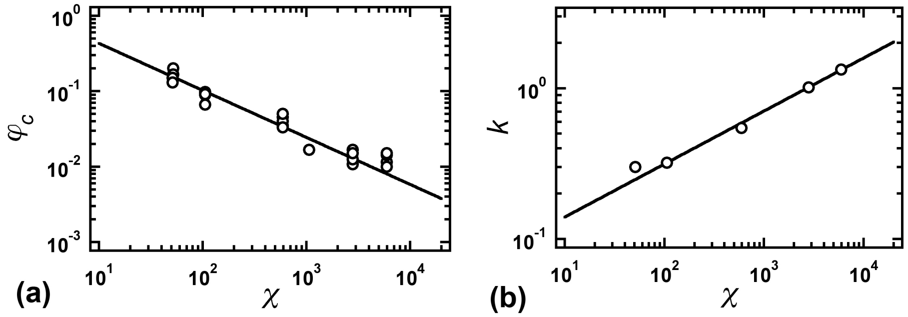

Figure 25: Influence of viscosity contrast $\chi$. (*a*)Critical flow rate ratio $\varphi_c$ for lubrication transition. Solid line: $\varphi_c = 1.8\chi^{-0.62}$. (*b*) Evolution of the prefactor $k$. Solid line: $k = 0.06\chi^{0.35}$

fact, the more viscous the thread is the more it folds when it enters the diverging chamber, hence the thread folding amplitude $A$ increases with the viscosity ratio $\chi$. The smooth transition at low $\chi$ is interpreted as a partial lubrication failure. The system can readily integrate the two states (threading and piling) for low $\chi$ because the thread is relatively less viscous and therefore can ”re-flow” in the pile. For comparison, the Hele-Shaw cell approximation for $\chi$ (4.2) was plotted along with the amplitude change versus the flow rate ratio (Figure 23(a)). Upon carefully examining the transition for numerous flow rates and viscosity ratios, we define the lubrication transition to occur when $A/w = 0.3$, which, given our channel geometry ($w/h = 20$), corresponds to $A \approx 6h$.

Assuming the lubrication failure occurs when $A/w = 0.3$, we define the corresponding flow rate ratio as the critical flow rate ratio $\varphi_c$ which marks the transition between threading and piling for every viscosity contrast $\chi$ (Figure 25(a)). Fitting the data with a power law, the critical flow rate ratio $\varphi_c$ can be determined as a function of viscosity ratio $\chi$

$$\varphi_c = 1.8\chi^{-0.62}. \tag{4.3}$$

This simple law implies that the critical initial size $\varepsilon_c$ for a thread to traverse the chamber without piling decreases with the viscosity ratio $\chi$.

Although the thread size in the square channel is independent of the viscosity contrast $\chi$, in the square chamber the way in which the lubrication transition occurs suggests that there is a strong correlation between the envelope amplitude size of a lubricated thread and its viscosity contrast $\chi$. Assuming that the change in the thread size in the

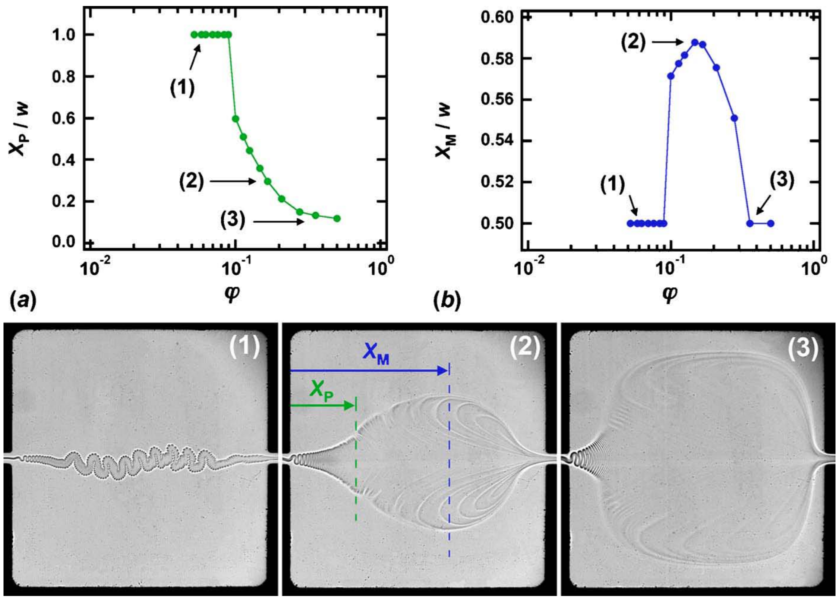

Figure 26: Morphological features of folding threads ($\chi = 106$). (*a*) Apparent penetration length of lubrication $X_P/w$ as a function of flow rate ratio $\varphi$. (*b*) Location of maximum amplitude $X_M/w$ for various $\varphi$. Bottom: corresponding experimental micrographs ($h = 100\ \mu$m, flow rates in $\mu$l/min): (1) $Q_1 = 10$, $Q_2 = 180$, (2) $Q_1 = 7$, $Q_2 = 40$, (3) $Q_1 = 5$, $Q_2 = 14$.

square chamber is also proportional to the square root of the flow rate ratio (3.1), we fit the amplitude of a folding lubricated thread in the chamber with

$$\frac{A}{w} = k\varphi^{\frac{1}{2}}, \tag{4.4}$$

where the prefactor $k$ is a function of the viscosity ratio. Data in Figure 25(b) are well fit by the function

$$k = 0.06\chi^{0.35}, \tag{4.5}$$

which yields an estimate of $A/w$ as a function of both $\varphi$ and $\chi$

$$\frac{A}{w} \approx c\chi^{\frac{1}{3}}\varphi^{\frac{1}{2}}, \tag{4.6}$$

where $c = 0.06$. This result indicates that the mean behavior of the system can be described using simple scaling laws, though the folding morphologies are rather intricate due to primary and secondary folding [49].

The lubrication failure can also be identified geometrically. Every lubricated thread starts folding upon entering the diverging section. However, if the system parameters lead to lubrication failure the thread eventually has to slow down due to the

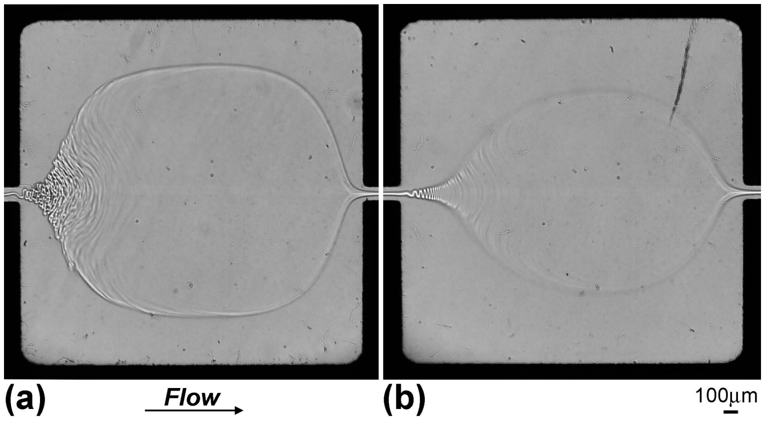

Figure 27: (a) First square chamber. (b) Second square chamber. $\varphi = 0.025$ and $\chi = 5933$.

viscous pile in the middle of the chamber (Figure 26 (2) and (3)). We define the length that the thread penetrates into the pile as the penetration length $X_P$. This length is normalized by the channel height and plotted as a function of flow rate ratio (Figure 26 (a)); $X_P/w = 1$ means that the thread was able to traverse the chamber as a lubricated thread, i.e. threading regime. Any $X_P/w < 1$ is an indication of lubrication failure which has started approximately around position $X_P$. Decreasing flow rate ratio $\varphi$ pushes the location of lubrication failure $X_P$ towards the second section of the chamber until $X_P$ is equal to the channel width and eventually $L1$ is a lubricated thread. In other words, increasing the side flow rate $Q_2$ helps pushing the more viscous liquid out of the channel.

Another geometrical parameter that helps in understanding the morphologies in the chamber and the lubrication mechanism is the location of the maximum central stream amplitude $X_M$. The lubrication failure is associated with an increase of the amplitude $A$ to conserve mass due to the reduction in the stream velocity resulting from the contact of the more viscous liquid $L1$ with the walls. Therefore, the location of the maximum amplitude $X_M$ indicates where the center of the pile is positioned. For a lubricated thread, the maximum is expected in the center of the chamber, where $tX_M/w = 0.5$, according to the single phase streamlines. The center of a fully formed pile is also expected in the middle of the chamber. During the transition, however, $X_M$ appears to shift toward the chamber outlet, as displayed in Figure 26 (b). The two parameters, $X_P$ and $X_M$, are useful indicators of the smooth lubrication transition for low $\chi$.

In some experiments, the square microchamber was followed by another similar chamber to observe the flow with the same flow rate ratio $\varphi$ after leaving the first chamber. Figure 27 shows that the same liquid pair with identical flow rate ratios have smaller envelop amplitude in the second chamber. Referring back to Figure 24, it is clear that fixing flow rate ratios, the envelope amplitude decreases with viscosity contrast. With that in mind, one can conclude that indeed the viscosity ratio has decreased in the second chamber, which is an indiction of mixing of the two PDMS oils.

## 4.3 Immiscible Core-Annular flow

Similar to miscible viscous core annular flow, the capillary threads of immiscible viscous core-annular flows also fold upon entering the diverging chamber. However, due to wetting and interfacial tension effects these threads behave quite differently further downstream. This difference is mainly due to the stability of the thin lubrication film of $L2$ between the thread and the walls. As was mentioned before, the liquid/liquid contact angle $\theta_{12}$ plays an important role on the morphologies in the square chamber which are made by the competing mechanisms, namely, the viscous folding and the capillary instabilities.

Microflows are examined in two situations: (a) for a nonwetting thread and (b) for a partially wetting thread. Fluid pairs were selected according to their mutual contact angle on borosilicate glass. For the nonwetting case, we used a silicone oil having a viscosity $\eta_1 = 485$ cP for $L1$ and ethanol for $L2$ ($\eta_2 = 1.16$ cP). The contact angle in this situation approaches $\theta_{12} \approx 180$ deg and a drop of $L1$ immersed in a continuous phase of $L2$ assumes a typical bead shape on the glass surface (Figure 28 (a)). Using the combined capillary rise method [50] with well-characterized borosilicate glass tubes, we measure the interfacial tension $\gamma_{12} = 1.7 \pm 0.2$ mN/m between $L1$ and $L2$. For the partially wetting case, a heavy mineral oil having a viscosity of $\eta_1 = 131$ cP for $L1$ and silicone oil for $L2$ ($\eta_2 = 6.5$) cP were used. The mean contact angle in this case is reported $\theta_{12} \approx 70$ deg [51], which is less than $\pi/2$.

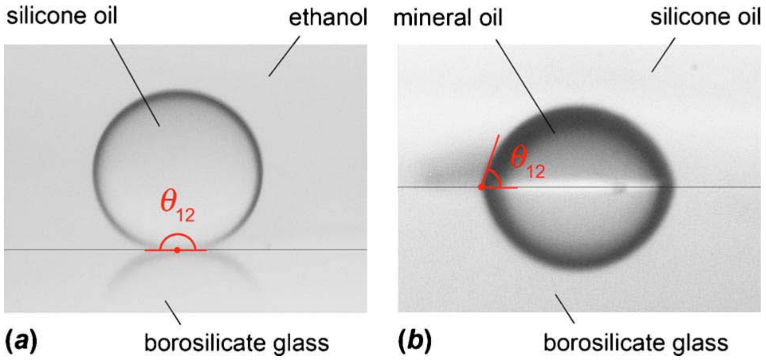

Figure 28: Liquid/liquid contact angle measurments on borosilicate glas. (a) $L1$: silicon oil, $L2$: ethanol, and $\theta_{12} \approx 180$ deg. (b) $L1$: heavy mineral oil, $L2$: silicon oil, and $\theta_{12} \approx 70$ deg.

### 4.3.1 Nonwetting Thread

Silicon oil and ethanol with the contact angle $\theta_{12} \approx 180$ deg and viscosity ratio $\chi = 419$ are used to study the behavior of non-wetting threads in the square chamber. The thin thread formed with this liquid pair can also traverse the chamber as a lubricated thread (Figure 29 (b)) flowing with certain flow rates. The capillary thread goes under primary and secondary folding (i.e., folding of a folded thread), and primary folds in the vicinity of one another coalesce along the flow direction. Consequently, a thicker thread is formed which has to unfold due to surface tension effects when exiting the chamber. However, unlike the miscible core-annular flow where thicker threads of $L1$ can touch the walls and form a pile in the middle of the chamber, due to the wetting situation between $L1$ and $L2$, when the folding amplitude $A$ grows the stable thin film of ethanol does not let silicon oil touch the walls. Therefore, the more viscous liquid has to breakup as chunks due to folding with large amplitudes (Figure 29 (c)). This intriguing breakup by folding regime has some direct practical applications since it provides new means for emulsifying high-viscosity fluids at large capillary numbers $Ca$. In these experiments, the capillary number is

$$Ca = \frac{\eta_1(Q_1 + Q_2)}{\gamma_{12}h^2}, \tag{4.7}$$

calculated based on the inlet flow in the square microchannel.

Capillary number $Ca$ allows for nondimensionalizing the flow velocity, which, in contrast with weakly diffusive threads, strongly influences flow morphologies. Figure 29

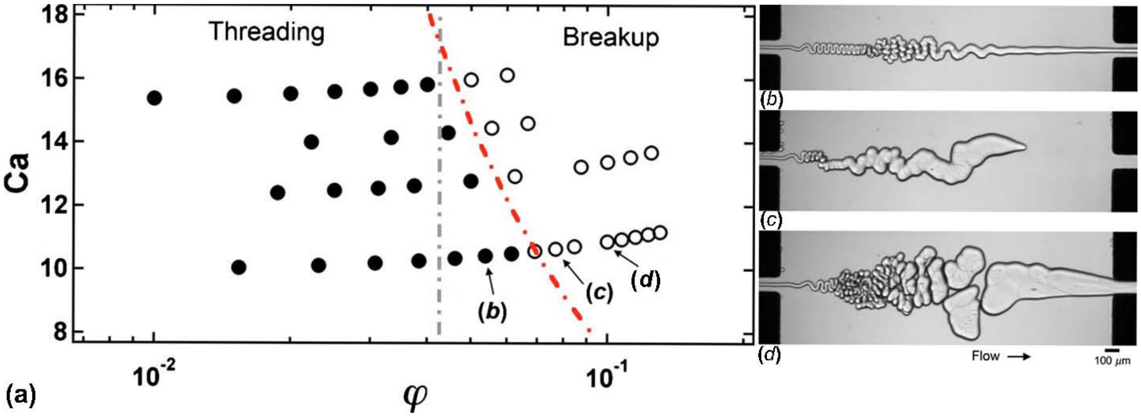

Figure 29: Deformation of non-wetting threads made of silicone oil in a sheath of ethanol ($\chi$= 419). (a) Phase-diagram of flow regimes, $Ca$ vs. $\varphi$: threading (•), break-up (○). Gray dash-dot line: Critical flow rate ratio $\varphi_c = 0.043$ for the lubrication transition of miscible threads having similar $\chi$. Red dash-dot line: $\varphi_c = 0.7Ca^{-1}$. Micrographs of threading and breakup regimes, flow rates in $\mu$l/min, $Q_2 = 130$: (b) $Q_1 = 7$, (c) $Q_1 = 10$, (d) $Q_1 = 13$.

(a) shows the flow map and transition line between threading and breakup regimes. The critical flow rate ratio $\varphi_c$ for the transition depends on the capillary number $Ca$ and we empirically find that the function

$$\varphi_c = 0.7Ca^{-1} \tag{4.8}$$

fits data reasonably well over the range of parameters investigated. Using our previous finding with miscible threads (4.3) the transition between threading and breakup in the case of no surface tension effects can also be roughly estimated based on the fluid viscosity ratio of this particular case. Assuming a miscible fluid pair with the same viscosity ratio $\chi = 419$, the equivalent critical flow rate ratio for threading/piling would be $\varphi_c = 4.2 \times 10^2$, which appears to asymptotically match data for the threading/breakup transition at large $Ca$ when viscous forces are predominant (gray dash-dot line in Figure 29 (a)).

### 4.3.2 Partially Wetting Thread

The results of a partially wetting thread (where $L1$ is made of heavy mineral oil and $L2$ is made of silicone oil, contact angle $\theta_{12} = 70$ deg, and viscosity ratio $\chi = 20$) [51] show that the system constantly encounters a competition between wetting and encapsulation mechanisms. Unlike the nonwetting thread where the stable thin layer of $L2$

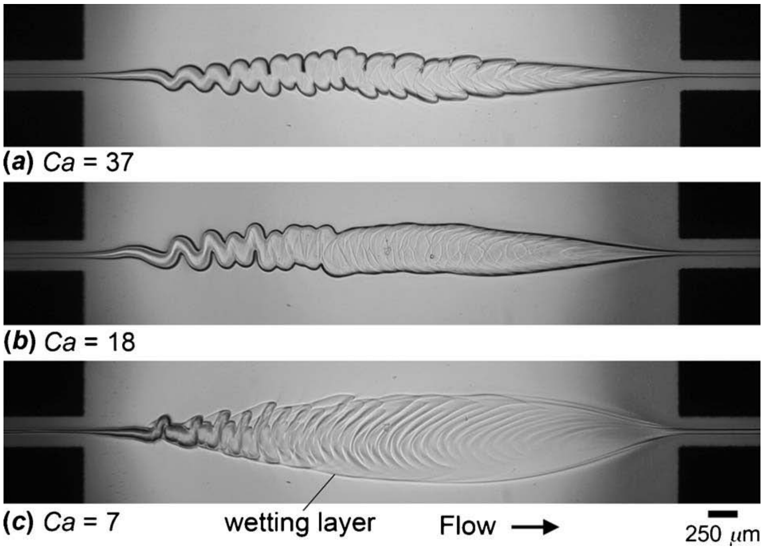

Figure 30: Influence of injection capillary number $Ca$ and wetting transition for fixed flow rate ratio: $\varphi = 5 \times 10^{-2}$ between heavy mineral oil (thread) and silicone oil (sheath). Flow rates in $\mu$l/min: (a) $Q_1 = 5$, $Q_2 = 100$, $Ca = 37$; (b) $Q_1 = 2.5$, $Q_2 = 50$, $Ca = 18$; (c) $Q_1 = 1$, $Q2 = 20$, $Ca = 7$

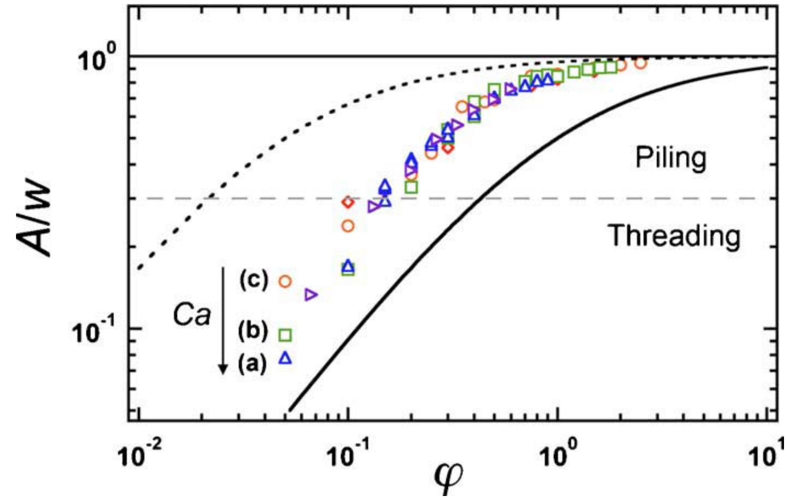

Figure 31: Evolution of the normalized envelope amplitude $A/w$ for partially wetting threads as a function of the flow rate ratio $\varphi$ for various fixed side flow rate (in $\mu$l/min) $Q2 = 10(\diamond)$, $20(\circ)$, $50(\square)$, $100(\triangle)$, $150(\triangleright)$ . (a), (b), and (c) correspond to data in Figure 30. Solid line: $A/w = [1+\varphi^{-1}]^{-1}$, dashed-line: $A/w = [1+(\chi\varphi)^{-1}]^{-1}$, gray line: $A/w = 0.3$

prevents $L1$ from touching the walls, in the situation of partially wetting threads there is a possibility of the substitution of the $L2$ lubricating layer by a $L1$ wetting layer.

Similar to the nonwetting thread, capillary number $Ca$ plays an important role on the flow morphologies in the chamber. For low $Ca$, $L1$ can replace $L2$ and form a

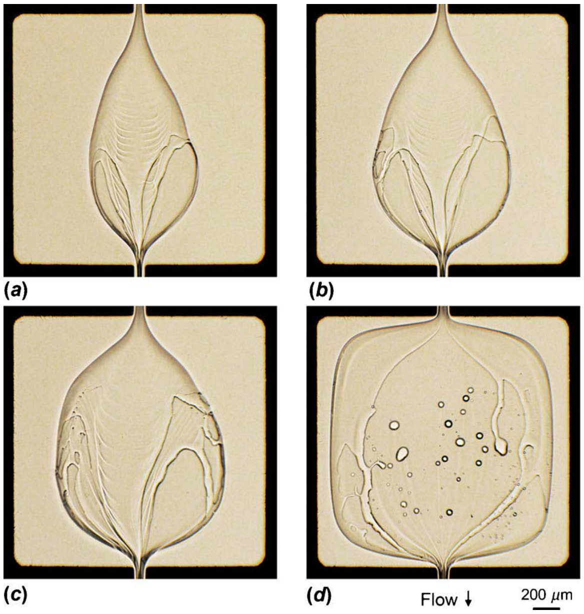

Figure 32: Dewetting flow patterns between heavy mineral oil (thread) and silicone oil (sheath). Flow rates in $\mu$l/min. (a) $Q_1 = 1.5$, $Q_2 = 5.4$, $\varphi = 0.28$, $Ca = 2.4$; (b) $Q_1 = 1.5$, $Q_2 = 4$, $\varphi = 0.37$, $Ca = 1.9$; (c) $Q_1 = 1.5$, $Q_2 = 3$, $\varphi = 0.5$, $Ca = 1.6$; (d) $Q_1 = 5$, $Q_2 = 2$, $\varphi = 2.5$, $Ca = 2.5$

pile in the middle of the chamber (Figure 30 (c)). For larger $Ca$, $L1$ is lubricated by $L2$ due to the dominant viscous effects (Figure 30 (a)). Therefore, the size of the average envelope amplitude normalized by channel width $A/w$, again, can be used as a phase change indicator from piling to threading(Figure 31).

In case of partially wetting threads, low capillary numbers ($Ca \leq 2.5$) significantly effect the pile morphologies [51]. In this case, the interfacial tension effects are dominant and they even prevent any folding of the thread upon entering the chamber. The growth of dewetting patches is the main characteristic of this type of flow (Figure 32). Increasing the flow rate ratio $\varphi$ leads to larger dewetting patches. In some cases, the rupture in the $L2$ layer can occur so fast that some droplets can stick to the wall and never get connected with the $L2$ stream (Figure 32 (d)).

# 5 Conclusion and Future Work

In this investigation, the viscous core-annular flow of miscible and immiscible fluids was discussed. First, single phase flow in a Hele-Shaw cell was used to characterize the flow in a square chamber. Then flow morphologies of weakly diffusive viscous core-annular flows were classified into two regimes: threading and piling for thin and thick viscous threads, respectively. The change in the size of the envelope amplitude was shown as a function of the flow rates $Q_1$ and $Q_2$ and the viscosity ratio $\chi = \eta_1/\eta_2$. The lubrication transition occurs when $A/w \approx 0.3$ and the critical flow rate for a specific viscosity contrast can be found through a simple scaling law. In the threading regime, the envelope amplitude was characterized as a function of $\varphi$ and $\chi$ which shows directly how viscosity effects the behavior of viscous threads. Lubrication failure can be determined from two geometrical parameters derived directly from the experimental images.

In the case of immiscible fluids, the behavior of the nonwetting threads was compared with the partial wetting case. It was found that thick nonwetting threads can breakup into chunks due to the presence of the stable thin layer of $L2$ at the walls, and the thinner threads can unfold due to capillary effects. The partially nonwetting threads can also exhibit threading or piling depending on the capillary number $Ca$.

The study of core-annular flow can help in understanding the complicated behavior of two phase flows and contribute to the fundamental study of two liquid flows. In addition, knowing the nature of these intriguing phenomenon can lead to ingenious inventions. The effect of geometry should also be taken into account for future studies as well as exploring the capillary thread in wider viscosity ranges.

In addition to the study of highly viscous liquids, the micromachining of microstructures with an ultrafast laser was examined. The microchannel etched with the laser and sealed with fusion bonding was tested to prove that this method can produce microchannels. Then the laser was calibrated with three different materials, and the channel width was predicted with a Gaussian distribution beam diameter. Also, the channel heights on each material were plotted as a function of a nondimensionalized number $\Omega$. The results of all materials collapsed on a single curve and showed that channel height changes linearly with Ω.

For further studies, the effect of interfacial tension along with the viscosity contrast should be investigated more thoroughly for various fluid pairs in different chamber geometries. Also, it would be an effective way to prove the quality of laser fabricated microchannels by fabricating similar microchannels used for the current study with an ultrafast laser and comparing the results of these two cases.

# Acknowledgments

It has been a great honor to work in Microfluidics lab at Stony Brook University. Samira Darvishi gratefully acknowledges the infinite support of Professor Thomas Cubaud in the past three years. She is confident that writing the current manuscript has helped her grown in many dimensions and is looking forward to observe, learn and work more than before.

The current research was supported by the National Science Foundation through grant CBRT 0932925.

# References

[1] F.A. Gomez. *Biological applications of microfluidics*. Wiley-Interscience, 2008.

[2] George M. Whitesides. What comes next? *Lab Chip*, 11:191–193, 2011.

[3] Holger Becker. Mind the gap! *Lab Chip*, 10:271–273, 2010.

[4] Holger Becker. All i want for christmas... *Lab Chip*, 11:1571–1573, 2011.

[5] J. El-Ali, P.K. Sorger, and K.F. Jensen. Cells on chips. *Nature (London)*, 442:403–411, 2006.

[6] J.W. Hong, V. Studer, G. Hang, W.F. Anderson, and S.R. Quake. A nanoliter-scale nucleic acid processor with parallel architecture. *Nature biotechnology*, 22(4):435–439, 2004.

[7] M. Toner and D. Irimia. Blood-on-a-chip. *Annu. Rev. Biomed. Eng.*, 7:77–103, 2005.

[8] Won-Gun Koh and Michael Pishko. Immobilization of multi-enzyme microreactors inside microfluidic devices. *Sensors and Actuators B: Chemical*, 106(1):335 – 342, 2005. ISOEN 2003 - Selected Papers from the 10th International Symposium on Olfaction and Electronic Noses.

[9] N.T. Nguyen and Z. Wu. Micromixersa review. *Journal of Micromechanics and Microengineering*, 15:R1, 2005.

[10] T. Kawakatsu, H. Komori, M. Nakajima, Y. Kikuchi, and T. Yonemoto. Production of monodisperse oil-in-water emulsion using cross flow-type silicon microchannel plate. *J. Chem. Eng. Japan*, 32:241–244, 1999.

[11] L.G. Leal. Flow induced coalescence of drops in a viscous fluid. *Physics of fluids*, 16:1833, 2004.

[12] S.L. Anna, N. Bontoux, and H.A. Stone. Formation of dispersions using ”flow focusing” in microchannels. *App. Phys. Lett.*, 82:364–366, 2003.

[13] Q. Xu and M. Nakajima. The generation of highly monodisperse droplets through the breakup of hydrodynamically focused microthread in a microfluidic device. *App. Phys. Lett.*, 85:3726–3728, 2004.

[14] T. Cubaud, M. Tatineni, X. Zhong, and C.-M. Ho. Bubble dispenser in microfluidic devices. *Phys. Rev. E*, 72:037302, 2005.

[15] P. Garstecki, M. Fuerstman, H.A. Stone, and G.W. Whitesides. Formation of droplets and bubbles in a microfluidic t-junction-scaling and mechanism of breakup. *Lab Chip*, 6:437–446, 2006.

[16] A.S. Utada, A. Fernandez-Nieves, H.A. Stone, and D.A. Weitz. Dripping to jetting transitions in coflowing liquid streams. *Phys. Rev. Lett.*, 99:094502, 2007.

[17] Gregory A. Cooksey, Christopher G. Sip, and Albert Folch. A multi-purpose microfluidic perfusion system with combinatorial choice of inputs, mixtures, gradient patterns, and flow rates. *Lab Chip*, 9:417–426, 2009.

[18] J. Tanner Nevill, Alexander Mo, Branden J. Cord, Theo D. Palmer, Mu-ming Poo, Luke P. Lee, and Sarah C. Heilshorn. Vacuum soft lithography to direct neuronal polarization. *Soft Matter*, 7:343–347, 2011.

[19] Ingmar H. Riedel-Kruse, Alice M. Chung, Burak Dura, Andrea L. Hamilton, and Byung C. Lee. Design, engineering and utility of biotic games. *Lab Chip*, 11:14–22, 2011.

[20] P.G. Gennes, F. Brochard-Wyart, and D. Quéré. *Capillarity and wetting phenomena: drops, bubbles, pearls, waves*. Springer, 2004.

[21] J. Atencia and D.J. Beebe. Controlled microfluidic interfaces. *Nature*, 437(7059):648–655, 2004.

[22] D.B. Wolfe, R.S. Conroy, P. Garstecki, B.T. Mayer, M.A. Fischbach, K.E. Paul, M. Prentiss, and G.M. Whitesides. Dynamic control of liquid-core/liquid-cladding optical waveguides. *Proc. Nat. Acad. Sci.*, 101:12434–12438, 2004.

[23] X. Mao, J.R. Waldeisen, B.K. Juluri, and T.H. Huang. Hydrodynamically tunable optofluidic cylindrical microlens. *Lab Chip*, 7:1303–1308, 2007.

[24] S.K.Y. Tang, C.A. Stan, and G.M. Whitesides. Dynamically reconfigurable liquid-core liquid-cladding lens in a microfluidic channel. *Lab Chip*, 8:394–401, 2008.

[25] L. Mahadevan, W.S. Ryu, and A.D.T. Samuel. Fluid'rope trick'investigated. *Nature*, 392(6672):140–140, 1998.

[26] NM Ribe, HE Huppert, MA Hallworth, M. Habibi, and D. Bonn. Multiple coexisting states of liquid rope coiling. *Journal of Fluid Mechanics*, 555(-1):275–297, 2006.

[27] GM Homsy. Viscous fingering in porous media. *Annual Review of Fluid Mechanics*, 19(1):271–311, 1987.

[28] N.M. Ribe. Periodic folding of viscous sheets. *Physical Review E*, 68(3):036305, 2003.

[29] É. Guyon. *Physical hydrodynamics*. Oxford University Press, 2001.

[30] Y. Xia and G.M. Whitesides. Soft lithography. *Annual Review of Materials Science*, 28(1):153–184, 1998.

[31] P. G. Saffman and Geoffrey Taylor. The penetration of a fluid into a porous medium or hele-shaw cell containing a more viscous liquid. *Proceedings of the Royal Society of London. Series A, Mathematical and Physical Sciences*, 245(1242):pp. 312–329, 1958.

[32] G.K. Batchelor. *An introduction to fluid mechanics*. Cambridge University Press, New York, 1967.

[33] F.M. White. *Fluid Mechanics*. Mcgraw-hill Series in Mechanical Engineering. McGraw-Hill, 2010.

[34] F.M. White. *Viscous fluid flow*. McGraw-Hill series in mechanical engineering. McGraw-Hill Higher Education, 2006.

[35] P. G. Drazin. *Introduction to Hydrodynamic Stability*, volume 1. Cambridge University Press, Sep 2002.

[36] T. Hayat, M. Nawaz, S. Asghar, and Awatif A. Hendi. Series solution for flow of a second-grade fluid in a divergentconvergent channel. *Canadian Journal of Physics*, 88(12):911–917, 2010.

[37] L. Rosenhead. The steady two-dimensional radial flow of viscous fluid between two inclined plane walls. *Proceedings of the Royal Society of London. Series A, Mathematical and Physical Sciences*, 175(963):pp. 436–467, 1940.

[38] D.D. Joseph and Y.Y. Renardy. *Fundamentals of Two-fluid Dynamics: Lubricated transport, drops, and miscible liquids*. Interdisciplinary applied mathematics. Springer-Verlag, 1993.

[39] T. Cubaud and T.G. Mason. Folding of viscous threads in diverging microchannels. *Phys. Rev. Lett.*, 96:114501, 2006.

[40] T. Cubaud, B.M. Jose, and S. Darvishi. Folded micro-threads: Role of viscosity and interfacial tension. *Physics of Fluids*, 23:042002, 2011.

[41] P.G. de Gennes. Wetting: statics and dynamics. *Reviews of Modern Physics*, 57(3):827, 1985.

[42] R. Dreyfus, P. Tabeling, and H. Willaime. Ordered and disordered patterns in two-phase flows in microchannels. *Physical review letters*, 90(14):144505, 2003.

[43] M.J. Madou. *Fundamentals of microfabrication: the science of miniaturization*. CRC, 2002.

[44] J.M. Khosrofian and B.A. Garetz. Measurement of a Gaussian laser beam diameter through the direct inversion of knife-edge data. *Appl. Opt*, 22(21):3406–3410, 1983.

[45] T. Cubaud and T.G. Mason. High-viscosity fluid threads in weakly diffusive microfluidic systems. *New J. Phys.*, 11:075029, 2009.

[46] T. Cubaud and T.G. Mason. Capillary threads and viscous droplets in square microchannels. *Phys. Fluids*, 20:053302, 2008.

[47] P. Gondret and M. Rabaud. Shear instability of two-fluid parallel flow in a hele-shaw cell. *Phys. Fluids*, 9:3267–3274, 1997.

[48] R.W. Fox, A.T. McDonald, and P.J. Pritchard. *Introduction to fluid mechanics*. Wiley, 2008.

[49] T. Cubaud and T.G. Mason. Formation of miscible fluid microstructures by hydrodynamic focusing in plane geometries. *Phys. Rev. E*, 78:056308, 2008.

[50] N. Rashidnia, R. Balasubramaniam, and D. Del Signore. Interfacial tension measurement of immiscible liquids using a capillary tube. *AIChE J.*, 38:615–618, 1992.

[51] S. Darvishi and T. Cubaud. Lubrication of Highly Viscous Core-Annular Flows in Microfluidic Chambers. *Journal of Fluids Engineering*, 133:031203, 2011.